Determination of responses of liquid xenon to low energy electron and nuclear recoils using a PandaX-II detector[*]

Binbin Yan(燕斌斌)[1,4†]   Abdusalam Abdukerim(阿布都沙拉木·阿布都克力木)[1]   Wei Chen(陈葳)[1]

Xun Chen(谌勋)[1,4‡]   Yunhua Chen(陈云华)[5]   Chen Cheng(程晨)[6]   Xiangyi Cui(崔祥仪)[7]   Yingjie Fan(樊英杰)[8]

Deqing Fang(方德清)[9]   Changbo Fu(符长波)[9]   Mengting Fu(付孟婷)[10]   Lisheng Geng(耿立升)[11,12]   Karl Giboni[1]

Linhui Gu(顾琳慧)[1]   Xuyuan Guo(郭绪元)[5]   Ke Han(韩柯)[1]   Changda He(何昶达)[1]   Di Huang(黄迪)[1]

Peiyao Huang(黄沛尧)[15]   Yan Huang(黄焱)[5]   Yanlin Huang(黄彦霖)[13]   Zhou Huang(黄周)[1]   Xiangdong Ji(季向东)[14]

Yonglin Ju(巨永林)[15]   Shuaijie Li(李帅杰)[7]   Jianglai Liu(刘江来)[1,7,4§]   Zhuoqun Lei(雷卓群)[15]

Wenbo Ma(马文博)[1]   Yugang Ma(马余刚)[9,2]   Yajun Mao(冒亚军)[10]   Yue Meng(孟月)[1,4]   Kaixiang Ni(倪恺翔)[1]

Jinhua Ning(宁金华)[5]   Xuyang Ning(宁旭阳)[1]   Xiangxiang Ren(任祥祥)[16]   Changsong Shang(商长松)[5]

Lin Si(司琳)[1]   Guofang Shen(申国防)[11]   Andi Tan(谈安迪)[14]   Anqing Wang(王安庆)[16]   Hongwei Wang(王宏伟)[2,17]

Meng Wang(王萌)[16]   Qiuhong Wang(王秋红)[3,2]   Siguang Wang(王思广)[10]   Wei Wang(王为)[6]

Xiuli Wang(王秀丽)[15]   Zhou Wang(王舟)[1,4]   Mengmeng Wu(武蒙蒙)[6]   Shiyong Wu(吴世勇)[5]

Weihao Wu(邬维浩)[1]   Jingkai Xia(夏经铠)[1]   Mengjiao Xiao(肖梦姣)[14,18]   Pengwei Xie(谢鹏伟)[7]   Rui Yan(严锐)[15]

Jijun Yang(杨继军)[1]   Yong Yang(杨勇)[1]   Chunxu Yu(喻纯旭)[8]   Jumin Yuan(袁鞠敏)[16]   Ying Yuan(袁影)[1]

Jianfeng Yue(樊英杰)[5]   Xinning Zeng(曾鑫宁)[1]   Dan Zhang(张丹)[14]   Tao Zhang(张涛)[1,4]   Li Zhao(赵力)[1,4]

Qibin Zheng(郑其斌)[13]   Jifang Zhou(周济芳)[5]   Ning Zhou(周宁)[1]   Xiaopeng Zhou(周小朋)[11]

(PandaX-II Collaboration)

[1]School of Physics and Astronomy, Shanghai Jiao Tong University, MOE Key Laboratory for Particle Astrophysics and Cosmology, Shanghai Key Laboratory for Particle Physics and Cosmology, Shanghai 200240, China
[2]Shanghai Institute of Applied Physics, Chinese Academy of Sciences, Shanghai 201800, China
[3]Key Laboratory of Nuclear Physics and Ion-beam Application (MOE), Institute of Modern Physics, Fudan University, Shanghai 200433, China
[4]Shanghai Jiao Tong University Sichuan Research Institute, Chengdu 610213, China
[5]Yalong River Hydropower Development Company, Ltd., 288 Shuanglin Road, Chengdu 610051, China
[6]School of Physics, Sun Yat-Sen University, Guangzhou 510275, China
[7]Tsung-Dao Lee Institute, Shanghai 200240, China
[8]School of Physics, Nankai University, Tianjin 300071, China
[9]Key Laboratory of Nuclear Physics and Ion-beam Application (MOE), Institute of Modern Physics, Fudan University, Shanghai 200433, China
[10]School of Physics, Peking University, Beijing 100871, China
[11]School of Physics, Beihang University, Beijing 100191, China
[12]International Research Center for Nuclei and Particles in the Cosmos & Beijing Key Laboratory of Advanced Nuclear Materials and Physics, Beihang University, Beijing 100191, China
[13]School of Medical Instrument and Food Engineering, University of Shanghai for Science and Technology, Shanghai 200093, China
[14]Department of Physics, University of Maryland, College Park, Maryland 20742, USA
[15]School of Mechanical Engineering, Shanghai Jiao Tong University, Shanghai 200240, China
[16]School of Physics and Key Laboratory of Particle Physics and Particle Irradiation (MOE), Shandong University, Jinan 250100, China
[17]Shanghai Advanced Research Institute, Chinese Academy of Sciences, Shanghai 201210, China
[18]Center for High Energy Physics, Peking University, Beijing 100871, China
[19]Key Laboratory of Nuclear Physics and Ion-beam Application (MOE), Institute of Modern Physics, Fudan University, Shanghai 200433, China

Abstract: We present a systematic determination of the responses of PandaX-II, a dual phase xenon time projection chamber detector, to low energy recoils. The electron recoil (ER) and nuclear recoil (NR) responses are calibrated, respectively, with injected tritiated methane or ^{220}Rn source, and with ^{241}Am-Be neutron source, in an energy range from 1-25 keV (ER) and 4-80 keV (NR), under the two drift fields, 400 and 317 V/cm. An empirical model is used to fit the light yield and charge yield for both types of recoils. The best fit models can describe the calibration data significantly. The systematic uncertainties of the fitted models are obtained via statistical comparison to the data.

I. INTRODUCTION

The nature of dark matter (DM) remains an intriguing physics question today. The direct search for an important class of dark matter candidate, the weakly interacting massive particles (WIMPs), has been accelerated by development in dual phase xenon time projection chambers (TPCs), such as PandaX-II [1], XENON-1T [2], and LUX [3]. In these detectors, a WIMP may interact with xenon nuclei via elastic scattering, depositing a nuclear recoil (NR) energy from few keV_{nr} to a few tens of keV_{nr}. γs or βs from internal impurities. The detector materials produce electron recoil (ER) background events with insignificant probabilities identified as the NR signals.

In a dual phase xenon TPC bounded by a cathode at the bottom in the liquid and an anode at the top in the gas, each energy deposition is converted into two channels, the scintillation photons and ionized electrons. The former is the so-called $S1$ signal. Electrons are subsequently drifted towards the liquid surface, and extracted into the gas region with delayed electroluminescence photons ($S2$) produced. Both $S1$s and $S2$s are collected by two arrays of photomultiplier tubes (PMTs) located at the top and bottom of the TPC. For a given event, the combination of $S1$ and $S2$ allows the reconstruction of the recoil energy and vertex, and the proportion of $S1$ and $S2$ serves as a significant discriminant for ER and NR. It is essential to determine the detector response via *in situ* calibration.

For the ER response, the injected sources used in PandaX-II, include tritiated methane (CH_3T), ^{220}Rn, and ^{83m}Kr. For NR calibration, an external ^{241}Am-Be (AmBe) neutron source was used. In this study, the detector responses are determined by fitting these data under the NEST2.0 [4] prescription.

The rest of this paper is organized as follows. In Sec. II, the detector conditions and calibration setups are introduced. In Sec. III, data processing and event selection cuts are presented. The response model simulation will be introduced in Sec. IV, followed by detailed discussions on the fits of the light yield and charge yield, before the conclusion in Sec. V.

II. CALIBRATION SETUP

The PandaX-II experiment, located at the China Jinping underground laboratory (CJPL) [5], was under operation from March 2016 to July 2019, with a total exposure of 132 ton·day for dark matter search. The operation was partitioned into three runs, Runs 9, 10, and 11 [6], with calibration runs interleaved in between. The detector contained 580-kg liquid xenon in its sensitive volume. The liquid xenon was continuously purified through two circulation loops, each connected to a getter purifier. The internal ER sources were injected through some loop. Two PTFE tubes, at 1/4 and 3/4 height of the TPC surrounding the inner cryostat, were used as the guide tube for the external AmBe source. The TPC drift field in Run 9 was 400 and 317 V/cm in Runs 10/11, corresponding to the maximum drift times 350, and 360 μs, respectively. The running conditions, key detector parameters, and event selection ranges for the calibration data sets are presented in Table 1.

A. Tritiated methane

Tritiated methane calibration was initially developed by a LUX experiment [7] and recorded an excellent internal low energy β events. The tritiated methane source used in the PandaX-II was procured from American Radio labeled Chemicals, Inc., with a specific activity of 0.1 Curie per mole of methane. The injection diagram is shown in Fig. 1. The tritiated methane bottle was immersed in a liquid-nitrogen cold trap, so that a controllable quantity of CH_3T gas can diffuse through a needle valve to the 100 mL mixing volume. The gas in the mixing volume was flushed with xenon gas into the detector.

The injection of tritium was performed in 2016 after Run 9, wherein approximately 5.4×10^{-10} mol of methane was loaded into the detector. The tritium events were distributed uniformly in the detector. Liquid xenon was constantly circulated at approximately 40 SLPM (standard liter of gas per minute) through the purifier. The duration for the calibration run was 44 days, and the later data set with an average electron lifetime of 706 μs is used as the ER calibration data.

We observed that the hot getters were inefficient to remove tritium with activity plateau at 10.2 μBq/kg. We performed an offline distillation campaign after the calibration to reduced the tritium activity to 0.049±0.005 μBq/kg in Runs 10/11 [6].

B. ^{220}Rn

^{220}Rn, a decay progeny of ^{232}Th, is a naturally occurring radioactive noble gas isotope. Because its half-life is 55 s, the probability to contaminate the liquid xenon TPC is insignificant, as initially demonstrated in XENON100 [8]. Details of ^{220}Rn calibration setup and operation in PandaX-II is presented in Ref. [9]. The injection system

Table 1. Summary of ER and NR calibration data sets and corresponding detector configurations. PDE, EEE, and SEG, respectively, are the photon detection efficiency, electron extraction efficiency, and single electron gain. The values and systematics uncertainties are from Ref. [6]. E_{drift} and $E_{extract}$ are the drift field and extraction field. The number of events correspond to the calibration data after all cuts, which are described in Sec. III.

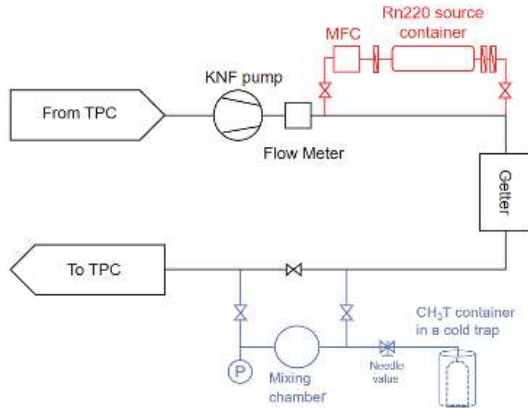| Data set	Run9 AmBe	Run9 Tritium	Runs 10/11 AmBe	Runs 10/11 ^{220}Rn
PDE	0.115±0.002		0.120±0.005	
EEE	0.463±0.014		0.475±0.020	
SEG	24.4±0.4		23.5±0.8	
E_{drift}/(V/cm)	400		317	
$E_{extract}$/(kV/cm)		4.56		
Livetime/d	6.7	27.9	48.5	11.9
Number of events	2902	9387	11196	8841
Drift time cut/μs	18-200	18-310	50-200	50-350
range cut	S1:3-150 PE S2:100-20000 PE	$E_{rec} < 25$ keV	S1:3-150 PE S2:100-20000 PE	$E_{rec} < 25$ keV

Fig. 1. (color online) Tritiated methane (blue) and ^{220}Rn (red) injection system. Tritiated methane injection system is installed downstream of the purifier to prevent chemical attachment to the purifier before entering into TPC.

consisting of a mass flow controller and a ^{232}Th source chamber with filters upstream and downstream, is shown in Fig. 1. In this injection, lantern mantles treated with thorium nitrate (Th(NO$_3$)$_4$) were used as the radon sources that gives a rate of 31.7 ± 0.3 Bq ^{220}Rn decays in the FV (define later in Sec. III). After ^{220}Rn was injected into the detector, the β-decay of the daughter nucleus ^{212}Pb gives uniformly distributed ER events with energy extending to zero. 11.9 days of ^{220}Rn data in 2018 are used as the low energy ER calibration for Runs 10/11.

C. AmBe

Neutron calibration data with an AmBe (α, n) source [10] with an approximate neutron emission rate of 2 Hz, producing an approximate 400 low energy nuclear recoils in the FV per day, were considered in Run 9 and Runs 10/11. The source was placed in the external calibration tubes. Calibration runs were recorded at eight symmetric locations in each loop to evenly sample the detector. For different source locations, no significant difference is identified in the detector response, therefore, we grouped the data in the analysis.

III. DATA SELECTION

The processing of the calibration data follows the procedure in Ref. [6]. Compared to the analyses [1, 11], seven unstable PMTs are inhibited from all data sets for consistency. This enhanced the PMT gain calibration, quality cuts, position reconstruction, and corresponding non-uniformity correction.

The raw $S1$ and $S2$ of each event is initially corrected for position non-uniformity based on the three-dimensional variation of the raw $S1$ and $S2$ for the uniformly distributed mono-energetic events, e.g. 164 keV (^{131m}Xe) owing to activation from the neutron source. The correction to $S1$ is a smooth three-dimensional hyper-surface. The correction to $S2$ is separated into an exponential attenuation vs. drift time (electron lifetime τ), and a smooth two-dimensional surface in the horizontal plane.

The electron equivalent energy of each event is reconstructed by

$$E_{rec} = W \times \left(\frac{S1}{PDE} + \frac{S2}{EEE \times SEG} \right), \tag{1}$$

where $W = 13.7$ eV [12] is the average energy to produce either a scintillation photon or free electron in liquid xenon, and PDE, EEE, and SEG, respectively, are the photon detection efficiency (ratio of detected photoelectrons to the total photons), electron extraction efficiency, and single electron gain, from the data (see Ref. [6] and Table 1). Recently, there is a new measurement of W in liquid xenon [13], yielding $W = 11.5 \pm 0.5$ eV, however, we used approximately 16% less. If we adopted the new

value, the PDE and EEE will increase by 16%, although the main effect in the response model in ($S1$, $S2$) will be scaled out.

Events with a single pair of $S1$ and $S2$ are selected. The fiducial volume (FV) definition is consistent with Ref. [6], except that a lower cut in drift time (200 µs) is applied to the AmBe data to prevent events that multi-scatter and deposit part of the energy in the below-cathode region, leading to suppressed $S2$ [11]. The lower selection cuts $S1 > 3$ PE and $S2_{raw} > 100$ PE are applied to all data sets. For the AmBe data, the upper selection cut is set at $S1 < 150$ PE (~ 80 keV$_{nr}$). For ER data, events with $E_{rec} < 25$ keV are selected. The vertex distributions of selected events are shown in Fig. 2, with FV cuts indicated. For all run sets, the bright bands at the maximum drift time (corresponding to cathode background) is constant at different radii. This is consistent with our COMSOL [14] simulation that predicts a better than 1% field uniformity throughout the FV. Therefore, in all later detector models, no field non-uniformity is considered.

The distributions of $S2$ vs. $S1$ for ER and NR events shown in Fig. 3 are used to determine the detector response model.

IV. DETERMINATION OF PANDAX-II RESPONSE MODELS

Our ER and NR response models is adapted from the prescription of NEST2.0 [4]. The light yield (L_y) and

charge yield (Q_y), defined as the number of initial quanta (photons or ionized electrons) per unit recoil energy, can be parameterized and fitted to the calibration data. The simulation models are discussed in Sec. IVA and Sec. IVB, and thereafter used for the data fitting in Sec. IVC

A. Quanta generation

For a distribution of true recoil energy from the calibration source, each recoil energy E_0 is converted into two types of quanta, scintillation photons n_{ph}^0 or ionized electrons n_e^0. For the NRs, the visible energy is quenched into $E_0 \times L$ owing to the unmeasurable dissipation of heat in the recoil, where L is the so-called Linhard factor from 0.1 to 0.25 for E_0 less than 100 keV$_{nr}$ [15].

For ER events, L is set to 1.0, to be consistent with the definition of W in [4]. Although this definition indicates that all ER energy is converted to photons or electrons, it considered as a convention rather than a fact, because some energy can be lost to other excitations.

The total quanta is given by

$$n_q \equiv n_{ph}^0 + n_e^0 = \frac{E_0 L}{W},$$
$$n_{ph}^0 = L_y E_0, \quad n_e^0 = Q_y E_0. \tag{2}$$

In NEST2.0, L_y is parameterized as an empirical function of $E_0 L$, and L_y and Q_y are related by Eq. (2). The intrinsic (correlated) fluctuations in n_e^0 and n_{ph}^0 is encoded

(a) Run 9 AmBe

(b) Runs 10/11 AmBe

(c) Run 9 tritium
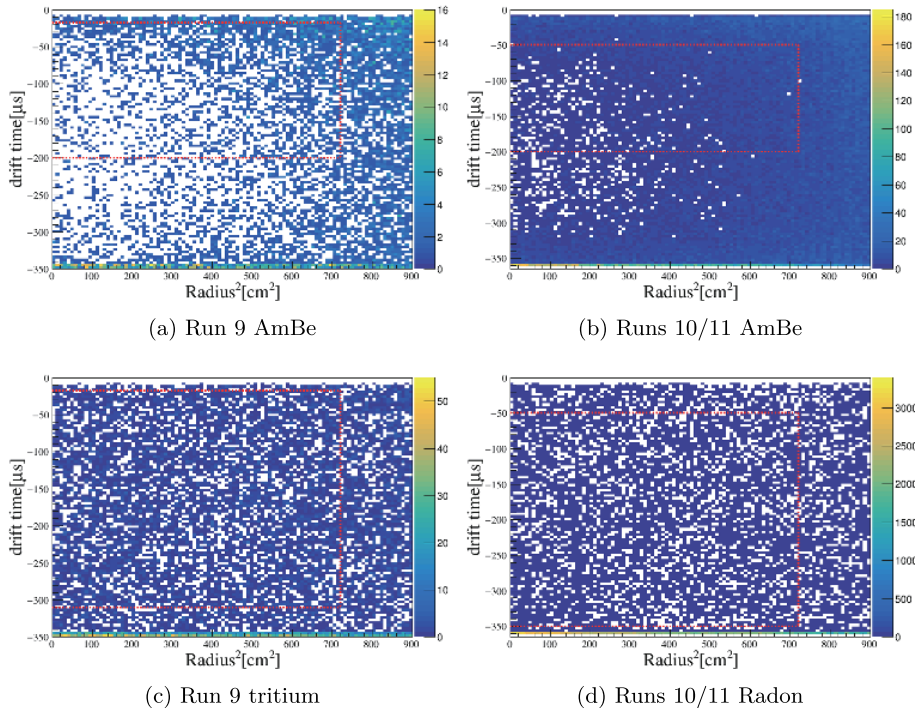

(d) Runs 10/11 Radon

Fig. 2. (color online) Event vertex distribution in drift time vs. radius-squared for each calibration data set. The FV region is indicated by dashed red line in each figure.
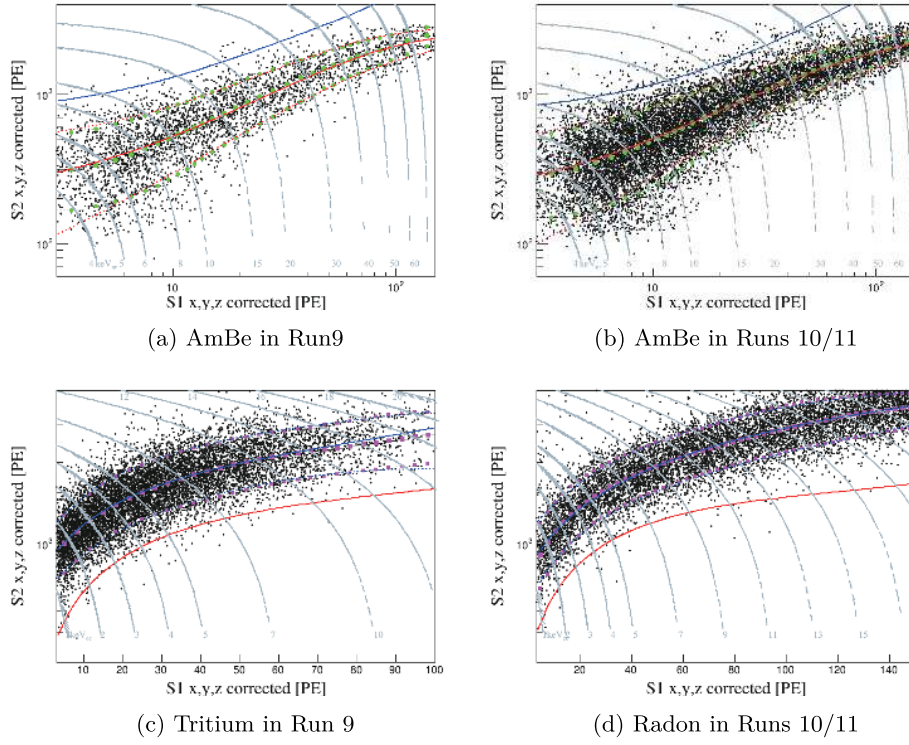
(a) AmBe in Run9

(b) AmBe in Runs 10/11

(c) Tritium in Run 9

(d) Radon in Runs 10/11

Fig. 3.   (color online) $S2$ vs. $S1$ of the selected calibration events. The red (blue) solid lines are the medians of NR (ER), and the red (blue) dashed lines refer to the 90% quantiles. For comparison, the 90% quantiles from the best fit response models (Sec. IV) are overlaid as the green (purple) dotted lines for NR (ER). The gray dashed curves are the equal-E_{nr} and equal-E_{rec} lines for the NR and ER events, respectively.

in our simulation by an energy dependent Gaussian smearing function $f(E_0L)$ as

$$n_e = \text{Gaus}(n_e^0, f(E_0L) \times n_e^0),$$
$$n_{ph} = n_q - n_e, \tag{3}$$

wherein $\text{Gaus}(\mu, \sigma)$ is a Gaussian random distribution with μ and σ as the mean and $\sigma=1$, and f is adjusted to the data (see Fig. 4). The smearing includes intrinsic fluctuations of the model and other time dependent systematic fluctuations of the detector.

B.   Model of the detector

The detector model is used to convert n_{ph} and n_e to detected $S1$ and $S2$. For the R11410-20 PMTs used in PandaX-II, the double-photoelectron emission probability by the 178 nm scintillation photons p_{2pe} is recorded as 0.21 ± 0.02 from the data [6]. Therefore, the total detected photons (N_{dph}) is given by

$$N_{dph} = \text{Binom}(n_{ph}, \text{PDE}/(1 + p_{2pe})), \tag{4}$$

in which $\text{Binom}(N, p)$ refers to a binomial distribution with N throws and a probability p, and $\text{PDE}/(1 + p_{2pe})$ is the binomial probability to detect a photon. N_{dph} is ran-

domly distributed onto the two arrays of PMTs (55 each) according to the measured top/bottom ratio from the data ($\sim 1:2$), to yield a significantly accurate simulation of the total PMT hits. Each detected photons is then fluctuated by p_{2pe}, leading to the total photoelectrons

$$N_{PE} = N_{dph} + \text{Binom}(N_{dph}, p_{2pe}). \tag{5}$$

$S1$ can be subsequently obtained by applying the single photoelectron (SPE) resolution, modeled as a Gaussian with a σ_{SPE} of 33% [16]

$$S1 = \text{Gaus}(N_{PE}, \sigma_{SPE} \times \sqrt{N_{PE}}). \tag{6}$$

Each $S1$ is required to have at least three hits, with each hit larger than 0.5 PE to simulate the single channel readout threshold and the multiplicity cut in the analysis [6].

Similarly, $S2$ is simulated based on n_e using detector parameters from the data. For each event, the drift time t_{drift} is randomized according to the data distribution, leading to an electron survival probability $s = \exp(-t_{drift}/\tau)$ with the electron lifetime τ obtained from the data. At the liquid level, the total electrons is
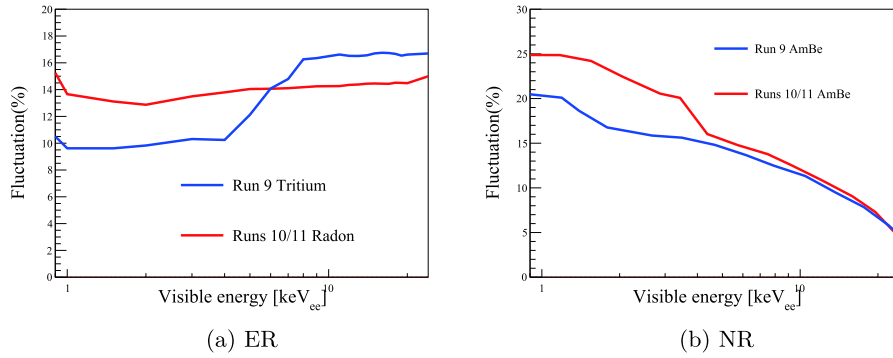
Fig. 4. (color online) The empirical fluctuation parameter *f* as a function of visible energy for the ER (left) and NR (right) data, both in electron equivalent energy keV$_{ee}$

$$N'_e = \text{Binom}(n_e, s). \qquad (7)$$

The total extracted electrons N''_e and $S2$ can be simulated as

$$
\begin{aligned}
N''_e &= \text{Binom}(N'_e, \text{EEE}), \\
S2 &= \text{Gaus}(N''_e \times \text{SEG}, \sigma_{\text{SE}} \times \sqrt{N''_e}),
\end{aligned} \qquad (8)
$$

where $\sigma_{\text{SE}} \sim 8.3$ PE is the Gaussian width for the single electron signals.

As discussed in Ref. [6], the nonlinearities in $S1$ and $S2$ owing to baseline suppression firmware are measured from the data, denoted by $f_1(S1)$ and $f_2(S2)$. So the detected $S1$ and $S2$ are

$$S1_d = S1 \times f_1, S2_d = S2 \times f_2. \qquad (9)$$

Finally, the data selection efficiency is parameterized as a Fermi-Dirac function

$$\epsilon(S1_d) = \frac{1}{1 + \exp\left(\dfrac{S1_d - p_0}{p_1}\right)}, \qquad (10)$$

where p_0 and p_1 are determined by fitting to calibration data. We observed that the $S2$ efficiency can be omitted, presumably owing to the large $S2_{\text{raw}} > 100$ PE selection cut that is signficantly above the trigger threshold of 50 PE [17]. The final efficiency at high energy end is absorbed in this analysis by normalizing the data with the simulation.

C. Extraction of parameters in the response model

In this section, the ER and NR response models will be fitted against the calibration data in $S1$ and $S2$ using unbinned likelihood. The systematic uncertainties of the models are quantified by a likelihood ratio approach.

1. *The likelihood function*

As an initial approximation, L_y can be fitted from the medians of the calibration data distribution by

$$L_y^0(E_{\text{rec}}/L) = \frac{S1}{\text{PDE} \times E_{\text{rec}}/L}, \qquad (11)$$

where E_{rec} (Eq. (1)) is the reconstructed energy including all detector effects, and the $\dfrac{E_{\text{rec}}}{L}$ is the estimate of E_0. The true L_y can be parameterized as

$$L_y(E_0) = L_y^0(E_0) + \sum_{n=0}^{4} c_n P_n(E_0), \qquad (12)$$

in which $P_n(E_0)$ is the nth order Legendre polynomial functions, and c_n can be fitted to data.

For a given model, a two-dimensional probability density function (PDF) in ($S1,S2$) is produced with a large statistics simulation described in Secs. IVA and IVB using the following sets of parameters: a) PDE, EEE and SEG constrained by their Gaussian priors (Table 1), with the anti-correlation between PDE and EEE embedded (see Ref. [18]), b) parameters for $\epsilon(S1_d)$ in Eq. (10), with a flat sampling of $p_0 \in (2,5)$ and $p_1 \in (0,1)$, respectively, and c) a 4th order Legendre polynomial expansion for L_y in Eq. (12), with $c_n(n = 0, 1, 2, 3, 4)$ uniformly sampled from -5 to 5. Experiments were performed to investigate if the polynomial expansion converges after the 3rd power. Parameters such as the fluctuation in the electron lifetime and, that are independently determined from the data were fixed in the simulation. For the baseline suppression nonlinearities, the smooth probability distributions determined from the data in Ref. [6] are sampled.

To compare the data to the PDF, a standard unbinned log likelihood function is defined in the space of ($S1,S2$) as

$$-2\ln\mathcal{L} = \sum_{i=1}^{N} -2\ln(P(S1^i, S2^i)), \qquad (13)$$

where $P(S1^i, S2^i)$ is the probability density for a given calibration data point i, and N is the total number of events for each calibration data set.

2. *The best fit and allowable parameter space*

An independent parameter scan is performed to determine the best fit model for each calibration data set. The best fit corresponds to the PDF that yields the minimum $-2\ln\mathcal{L}$. For illustration, the centroids and 90% quantiles of the best fit models from the four data sets are shown in Fig. 3, where the data are consistent.

The parameter space allowable by the calibration data is determined based on the likelihood ratio approach in Ref. [19]. For each set of fixed parameters, 1000 mock data runs are produced with equal although Poisson fluctuated statistics as the calibration data. The test statistic for each mock run is defined as the difference between the log likelihood calculated using the fixed point PDF, and the global minimum value from the parameter scan as,

$$\Delta\mathcal{L} = -2\ln\mathcal{L}_{\text{fixed}} - (-2\ln\mathcal{L}_{\text{min}}). \qquad (14)$$

The distributions of $\Delta\mathcal{L}$ for the mock data generated from the best fit parameters for the four calibration data sets are shown in Fig. 5. The blue dashed regions refer to the 90% integrals from zero, beyond which the difference between the mock data set and its own PDF is less likely. The 90% boundary values for $\Delta\mathcal{L}$ at other parameter space points are similar. Therefore, $\Delta\mathcal{L}$ of the real data is tested around the best fit, and the allowable space is defined by the 90% boundaries in Fig. 5. The corresponding allowable range of distributions in recoil energy, $S1$, and $S2$ are shown in Fig. 6, together with the calibration data that were consistent.

The resulting best fit Q_y and L_y for the NR and ER events are shown in Fig. 7, overlaid with the world data, and the native NEST2.0 predictions [4]. The shaded bands indicate the 90% allowable model space, with uncertainties owing to detector parameters and statistics of the calibration data naturally incorporated. Our NR models cover a wide energy range from 4 to 80 keV$_{\text{nr}}$. At the two drift fields (400 and 317 V/cm), our optimal NR models are consistent as expected. For the Q_y distribution with recoil energy from 4 to 15 keV$_{\text{nr}}$, there is significant spread among the world data, wherein our Q_y is significantly consistent with Ref. [20] (Xenon-1T 2019), although lower than others. The NEST2.0 global fit, predominantly driven by data from Ref. [21] (LUX DD), has a higher Q_y than that of our model. The global data con-

(a) AmBe in Run 9

(b) AmBe in Runs 10/11

(c) Tritium in Run 9
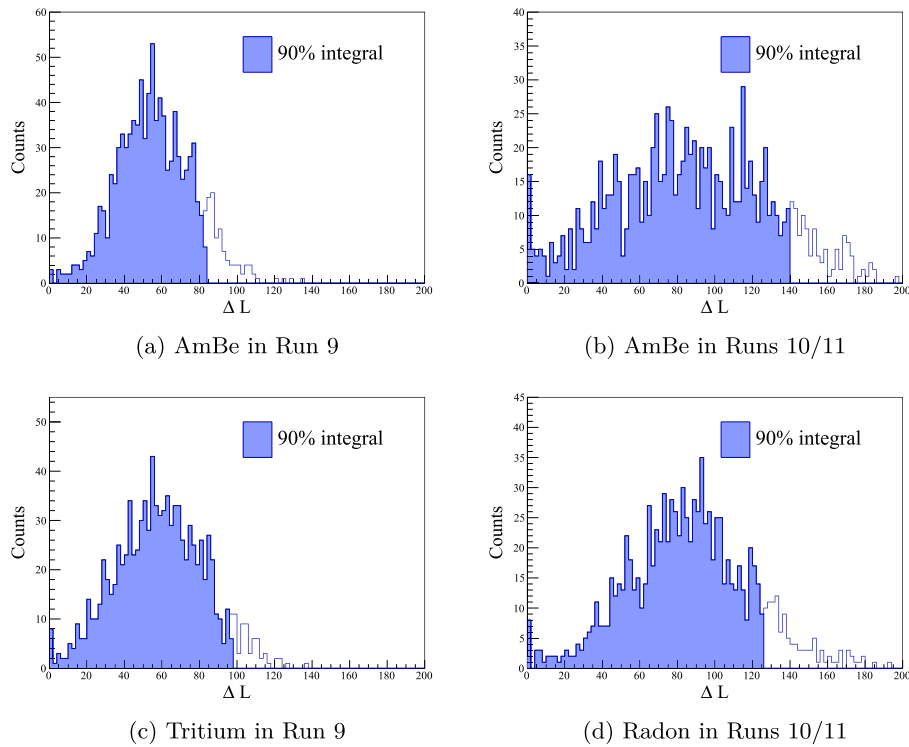

(d) Radon in Runs 10/11

Fig. 5.   (color online) The distribution of $\Delta\mathcal{L}$ for mock calibration data sets generated at the best fit parameter points. The shaded regions indicate the 90% integrals.
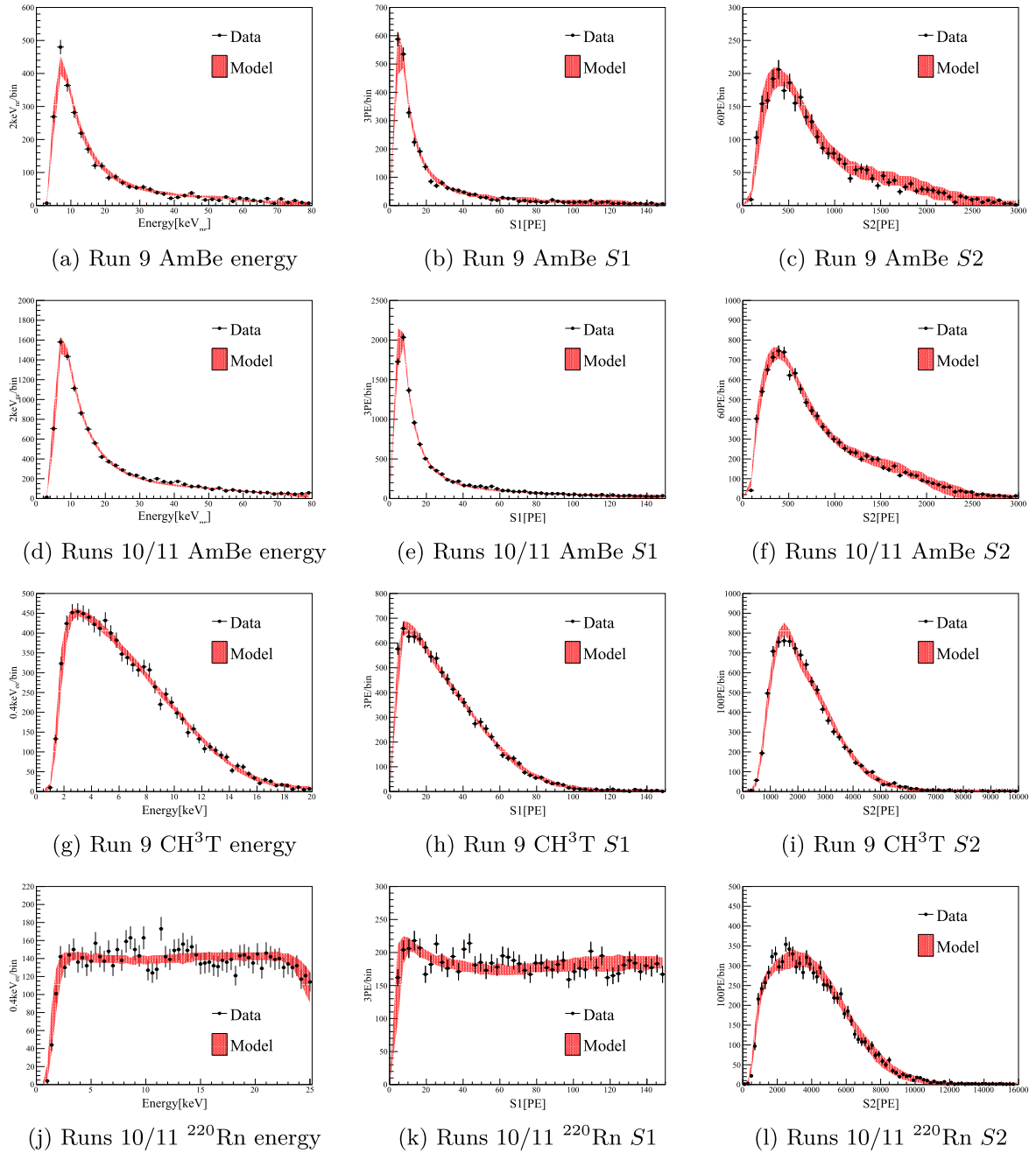
Fig. 6.   (color online) The comparison of calibration data (points) and model (shaded bands = 90% allowable) in the recoil energy, $S1$, and $S2$, in Run 9 and Runs 10/11. For the ^{220}Rn energy distribution (j), the decrease at high energy end is due to the 150 PE $S1$ range cut.

sistency improved significantly above 15 keV$_{nr}$. L_y of our NR models, in contrast, is consistent with most world data, except some insignificant tension at above 25 keV$_{nr}$ with Ref. [22] (Manzur 2010), which bears large uncertainties by itself.

For the ER models, Q_y (L_y) for Run 9 is higher (lower) than that for Runs 10/11. This behavior is expected because the initial ionized electrons are less likely to be recombined in stronger drift field. Our model at 400 V/cm is consistent with Ref. [23] (Xenon100) at similar

drift field, although there is some considerably insconsistency with Refs. [24, 25] (neriX 480 V/cm, Lin 424 V/cm). Our Q_y (L_y) at 317 V/cm is lower (higher) than the world data, including that from Ref. [21] (LUX) taken at 180 V/cm (and that from Ref. [20] at 81 V/cm, not drawn), and the native NEST2.0 predictions. The key systematic effects can cause the differences in our data interpretation. For example, the three-dimensional uniformity correction for $S1$ and $S2$, correlated with position reconstruction, can lead to uncertainties in the PDE and EEE.
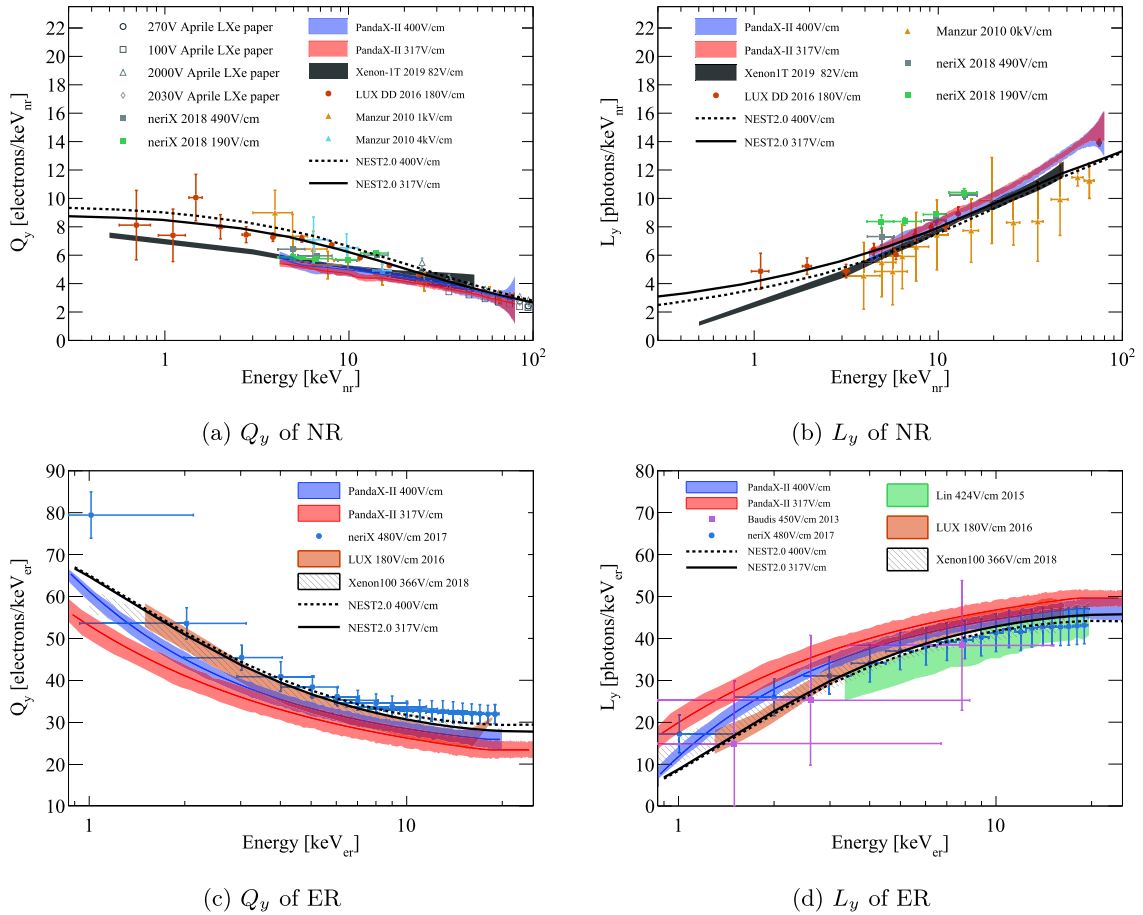
(a) Q_y of NR

(b) L_y of NR

(c) Q_y of ER

(d) L_y of ER

Fig. 7.   (color online) Charge yield Q_y (a) and light yield L_y (b) of the NR and Q_y (c) and L_y (d) of the ER obtained from the PandaX-II data: blue=400 V/cm, red=317 V/cm. Overlaid world data include: NR from Refs. [21, 22, 26-29], and ER from Refs. [7, 24, 25, 30], as indicated in the legend. The native NEST2.0 predictions are drawn in black curves, solid (317 V/cm), and dashed (400 V/cm). The XENON1T responses [20] are not included in the ER figures since the operation field (81 V/cm) is significantly different from the PandaX-II conditions, and for visual clarity.

At high energy, the saturation of PMTs and the after-pulsing under large S2s are also potential source of biases in these parameters. At low energy, the uncertainty of the selection efficiency, the BLS nonlinearity, and uncertainties in recoil energy distributions (particularly for NR events) can lead to systematics in the low energy response curves. Because most systematics can affect global measurements, investigations on systematics are desirable.

Notwithstanding the global comparison, for PandaX-II, models determined from *in situ* calibrations are the most self-consistent models to be used in the PandaX-II dark matter search data. Our best fit models presented herein have been adopted in the analysis in Ref. [6], with an overall uncertainty of 20% in the dark matter rate normalization to record global uncertainties.

V. CONCLUSION

We present an ER and NR responses from a PandaX-II detector based on calibration data from operation at two different drift fields (400 and 317 V/cm). The empirical best fits to the data and model uncertainties are obtained, indicating significant consistency between the data and our models. In comparison to those presented in Refs. [18, 31], the models in this work cover the entire PandaX-II data taking period, with a signficantly extended energy ranges from 4 to 80 keV$_{nr}$(NR) and 1 to 25 keV$_{ee}$(ER). At the two drift fields, our NR models are consistent, and our ER models exhibit a relative shift. Both behaviors are consistent with expectation.

Our models are also compared to some world data. Our NR models lie in the large global spread. For the ER response, our model yields a higher (lower) L_y (Q_y) in comparison to most world data, indicating some unaccounted systematic uncertainties in our or other measurements. These discrepancies encourage continuous calibration effort and further investigations of systematics in the data. Finally, the analysis approach presented herein is generalized and can be applied to similar noble liquid

TPC experiments.

References

[1]   A. Tan *et al*., Phys. Rev. D **93**(12), 122009 (2016), arXiv:1602.06563
[2]   E. Aprile *et al*., Eur. Phys. J. C **77**(12), 881 (2017), arXiv:1708.07051
[3]   D. S. Akerib *et al*., Phys. Rev. Lett. **112**, 091303 (2014)
[4]   M. Szydagis et al., https://doi.org/10.5281/zenodo.4283077. doi: 10.5281/zenodo.4283077.
[5]   Y.-C. Wu *et al*., Chin. Phys. C **37**(8), 086001 (2013), arXiv:1305.0899
[6]   Q. Wang *et al*., Chin. Phys. C **44**(12), 125001 (2020), arXiv:2007.15469
[7]   D. S. Akerib *et al*., Phys. Rev. D **93**(7), 072009 (2016), arXiv:1512.03133
[8]   E. Aprile *et al*., Phys. Rev. D **95**(7), 072008 (2017), arXiv:1611.03585
[9]   W. Ma *et al*., JINST **15**(12), P12038 (2020), arXiv:2006.09311
[10] Q. Wang *et al*., Sci. China Phys. Mech. Astron. **63**(3), 231011 (2020), arXiv:1907.00545
[11] X. Xiao *et al*., Phys. Rev. D **92**(5), 052004 (2015), arXiv:1505.00771
[12] M. Szydagis, N. Barry, K. Kazkaz *et al*., JINST **6**, P10002 (2011), arXiv:1106.1613
[13] G. Anton *et al*., Phys. Rev. C **101**(6), 065501 (2020), arXiv:1908.04128
[14] http://cn.comsol.com/.
[15] B. Lenardo, K. Kazkaz, A. Manalaysay *et al*., IEEE Transactions on Nuclear Science **62**(6), 3387-3396 (2015)
[16] S. Li *et al*., JINST **11**(02), T02005 (2016), arXiv:1511.06223
[17] Q. Wu *et al*., JINST **12**(08), T08004 (2017), arXiv:1707.02134
[18] X. Cui *et al*., Phys. Rev. Lett. **119**(18), 181302 (2017), arXiv:1708.06917
[19] G. Cowan, K. Cranmer, E. Gross *et al*., Eur. Phys. J. C **71**, 1554 (2011) [Erratum: Eur. Phys. J. C **73**, 2501 (2013)]. arXiv: 1007.1727, doi: 10.1140/epjc/s10052-011-1554-0.
[20] E. Aprile *et al*., Phys. Rev. D **99**(11), 112009 (2019), arXiv:1902.11297
[21] D. S. Akerib *et al*., *Low-energy (0.7-74 keV) nuclear recoil calibration of the LUX dark matter experiment using D-D neutron scattering kinematics (2016),* arXiv: 1608.05381
[22] A. Manzur, A. Curioni, L. Kastens *et al*., Phys. Rev. C **81**, 025808 (2010), arXiv:0909.1063
[23] E. Aprile *et al*., Phys. Rev. D **97**(9), 092007 (2018), arXiv:1709.10149
[24] L. Goetzke, E. Aprile, M. Anthony *et al*., Phys. Rev. D **96**(10), 103007 (2017), arXiv:1611.10322
[25] Q. Lin, J. Fei, F. Gao *et al*., Phys. Rev. D **92**(3), 032005 (2015), arXiv:1505.00517
[26] E. Aprile, C. Dahl, L. DeViveiros *et al*., Phys. Rev. Lett. **97**, 081302 (2006), arXiv:astro-ph/0601552
[27] P. Sorensen, JCAP **09**, 033 (2010), arXiv:1007.3549
[28] E. Aprile *et al*., Phys. Rev. D **88**, 012006 (2013), arXiv:1304.1427
[29] E. Aprile, M. Anthony, Q. Lin *et al*., Phys. Rev. D **98**(11), 112003 (2018), arXiv:1809.02072
[30] L. Baudis, H. Dujmovic, C. Geis *et al*., Phys. Rev. D **87**(11), 115015 (2013), arXiv:1303.6891
[31] A. Tan *et al*., Phys. Rev. Lett. **117**(12), 121303 (2016), arXiv:1607.07400